Design of a waveplate to generate circularly polarised XUV radiation

Contact *cephise.cacho@stfc.ac.uk*

Thorge Griffel

University of Applied Science Emden/Leer
Emden, 26723, Constantiaplatz 4, Germany

Cephise Cacho, Edmond Turcu, Emma Springate

Central Laser Facility
STFC, Rutherford Appleton Laboratory, Didcot, Oxon OX11 0QX, UK

Introduction

In the Artemis facility, soft XUV-radiation is generated in the energy region between 20 eV and 100 eV in order to perform time resolved photoemission experiments on condensed matter or gas phase targets. A fs laser beam is focused on a gas jet to generate high harmonics (HHG) of the fundamental beam. There is scientific interest in probing samples with circularly polarised XUV radiation. In the standard HHG process the photon produced are linearly polarised. Using oriented molecules, it is possible to generate polarised harmonics but with low efficiency and degree of polarization [1]. An alternative solution is to reflect the XUV beam on gold mirrors in order to introduce a phase shift between s- and p-polarization and so produce circularly polarised photons. We have designed a waveplate to produce circularly polarised XUV radiation at Artemis.

Theory and Calculation

It is well known that s- or p- polarised XUV photon beams have different reflectivities on Au mirrors. Furthermore, the phases of the reflected beam are different. Using multiple reflections on Au mirrors it is possible to transform linearly polarised XUV beams to circularly polarised beams. The purpose of this calculation is to determine the optimal angles for the mirrors. The intensity and phase of a reflected beam is contained in the reflection coefficient (complex number) defined by the Fresnel-equations.

$$\underline{r_s} = \frac{\cos(\varepsilon) - \sqrt{\tilde{n}^2 - \sin(\varepsilon)^2}}{\cos(\varepsilon) - \sqrt{\tilde{n}^2 - \sin(\varepsilon)^2}}$$

$$\underline{r_p} = \frac{\tilde{n}^2 * \cos(\varepsilon) - \sqrt{\tilde{n}^2 - \sin(\varepsilon)^2}}{\tilde{n}^2 * \cos(\varepsilon) - \sqrt{\tilde{n}^2 - \sin(\varepsilon)^2}}$$

where $\underline{r_s}$ ($\underline{r_p}$) is the reflection of an s (p)-polarised incident beam, ε the incidence angle, $\tilde{n} = \frac{n'}{n}$ the reflective index ratio (n': index of the material and n: index of the vacuum). The reflectivity and the phase of the reflected beam is obtained by calculating $R_{s(p)} = \left|\underline{r}_{s(p)}\right|^2$ and $\varphi_{s(p)} = Arg(\underline{r}_{s(p)})$. Finally, for an incident beam of linear polarisation with an angle α respect to the incident plane, the reflectivity and phase shift are given by

$$I = |\cos(\alpha) * R_s|^2 + \left|\sin(\alpha) * R_p\right|^2$$
$$\delta = \varphi_p - \varphi_s$$

All the following calculations are done with the complex refraction index for gold obtained from [2].

Reflectivity and Phase shift

As an example, we present in figure 1 the reflectivity and the phase shift after 4 reflections on gold mirrors. The incident beam is linearly polarised and the photon energy is 30 eV. Only the incidence angle region above 70 deg gives a large enough reflectivity for applications. The phase shift increases with the incident angle, crossing four angles (Fig1. red squares) where the beam is 100% circular polarised.

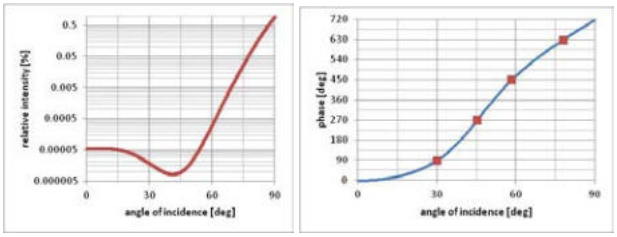

Figure 1: Calculation of the total reflectivity and phase shift after reflections on four gold mirrors. The photon energy is 30 eV and the results are plotted versus the incident angle. At grassing (78deg) incidence the reflected beam is fully polarised and the intensity maximal.

The optimal configuration to produce a fully circularly polarised beam would be at an incident angle of 77.9 deg giving a total reflectivity of 6.2 %.

Maximum Figure-of-merit configuration

According to fig.1 the reflectivity can be improved by increasing the incidence angle. This means a loss of the high degree of polarization for a higher intensity. The optimal compromise between the intensity and the degree of polarization is determined by the maximum of the figure of merit and it is given by the relation

$$f_{om} = R * (\tan\delta)^2$$

Where R is the reflectivity and $\tan(\delta)$ is the degree of circularly polarization (the 3rd normalised Stokes-Parameter [3-4]).

The maximum of the figure of merit gives us now the new position with an incidence angle of 83.5 degree giving a reflectivity of 24.5% and a degree of circular polarisation of 74.2%.

Results for 30eV up to 70eV photon energy

The same calculation was performed over the photon energy range of 30eV up to 70eV. In Figure 3, the reflectivity for a 100 % polarised beam (green curve) and for the maximum figure-of-merit (orange curve) are presented and reveal an increase of ~10% between both configurations.

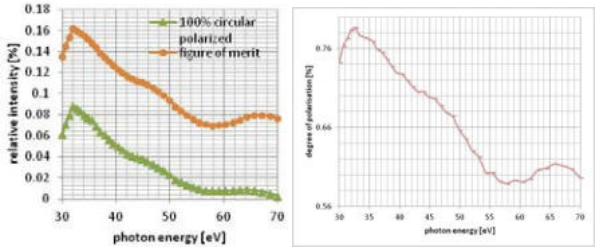

Figure 2: Variation of the reflectivity for a fully polarised beam and at the maximum of the figure-of-merit. Degree of polarisation corresponding to the maximum of the figure-of-merit.

Using the maximum of figure-of-merit, the optimal compromise between polarization and intensity is predicted to be when the polarization is reduced to the region 57 % - 77 % and giving a higher flux.

As the optical index of gold depends on the photon energy, the angles of the mirror have to be adjusted in order to control the total phase shift of the polariser. This can be calculated and Figure 3 presents the variation of the incidence angle for the fully polarised beam and for the maximum figure-of-merit.

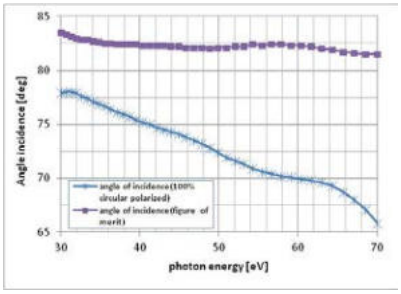

Figure 3: Variation of the incident angle versus the photon energy for a 100% circularly polarised beam (blue) and for the maximum of the figure of merit (purple)

Interestingly, in the case of the maximum figure-of-merit the incident angle does not vary much and could be kept fixed at 82.5 deg in experimental applications. This means the polarisation will vary with the photon energy (fig.2b) but the noise on the asymmetry measured will be optimal. Selection of either left or right handed polarisation will be achieved by rotating the polariser around the beam propagation direction.

Conclusions

This article describes the calculations for a waveplate built of four gold mirrors for XUV radiation in the photon energy range from 30eV to 70eV.

We can see high values for the relative intensity in the area between 30eV and 50eV for 100% circular polarised beams. For higher photon energies, the remaining intensity is very low. If a very high degree of polarisation is not necessary, the figure of merit method provides much more remaining intensity even for photon energies higher than 50eV. However, this has a cost in loss of polarisation.

Acknowledgements

The authors would like to thanks Dr. Cyrille Thomas and Dr. Hongchang Wang from Diamond Light Source for their help in the theoretical calculations of the reflectivity. T.G. would like to thank Professor, Prof. Dr. rer. nat. habil Ulrich Teubner from the university of applied science Emden/Leer, and Emma Springate, Cephise Cacho and Edmond Turcu from STFC, for supporting this project.

References

1. “Elliptically Polarized High-Order Harmonic Emission from Molecules in Linearly Polarized Laser Fields”, Xibin Zhou, Robynne Lock, Nick Wagner, Wen Li, Henry C. Kapteyn, and Margaret M. Murnane, JILA and Department of Physics, University of Colorado, Boulder 80309, USA (20 February 2009)
2. Centre of X-Ray Optics (CXRO) “http://henke.lbl.gov/optical_constants/” (December 2011)
3. “Optik für Ingenieure”, F. Pedrotti, L. Pedrotti, W. Bausch, H. Schmidt; Springer (3rd Edition)
4. “Polarized Vacuum Ultraviolet and X-Radiation”, James A. R. Samson, Behlen Laboratory of Physics, University of Nebraska, Lincoln, Nebraska 68588, USA

Laser beam pointing control system for driving the hollow-fibre few-cycle laser

Contact *thomas.kierspel@web.de*

Thomas Kierspel

Carl von Ossietzky University Oldenburg
Niedersachsen, Germany
University of Applied Sciences Emden Leer
Niedersachsen, Germany

Edmond Turcu, Klaus Ertel

Central Laser Facility, STFC Rutherford Appleton Laboratory
Didcot, UK

Introduction

At Artemis Facility a hollow-fibre compressor system is used to generate sub-10 fs pulses. The output signal of the hollow-fibre compressor is in terms of pulse duration and beam profile very sensitive to its input signal [1]. Hence a beam pointing stability control system has been developed to optimize the performance of the hollow-fibre compressor.

General Description

The pulse duration of the Red Dragon (KMLabs) laser system at Artemis is 30 fs. Some experiments require even shorter pulses. This goal is achieved at Artemis with a hollow-fibre compressor. A hollow-fibre compressor consists of a gas filled hollow-fibre which is used to broaden the spectrum and a compressor to compress the pulse afterwards. The process of spectral broadening is a non-linear process and is called "Self-phase modulation". The compressor consists of a set of chirped mirrors which impose each a group delay dispersion of ≈ – 45 fs^2. With this setup Dr. Willam Bryan achieved at Artemis pulse durations of 7 fs in May 2010 [2]. During the experiment the pulse duration was stable for approximately 20 minutes. After this time the pulse duration got longer and the beam profile was getting worse. This was due to the input beam of the hollow-fibre. A good coupling of the beam into the hollow fibre is very important to get a good output signal. The beam at the input of the hollow-fibre was moving slightly and thus a long-term stable output of the hollow-fibre compressor was not possible. Hence a pointing stability control system has been developed to achieve this goal.

Beam Pointing Stabilization Setup

In Figure 1 the setup of the beam pointing stabilization system (BPS) is shown. The incident laser pulse is focused onto the hollow-fibre with a silver-layered focussing mirror (f = 1.25 m). A part of the focused beam is taken form a leaky mirror to use as control for the camera. The camera (AVT Stingray) is placed at the same distance from the focussing mirror as the entrance of the hollow fibre. It is equipped with a 10x microscope objective (Edmund Optics).

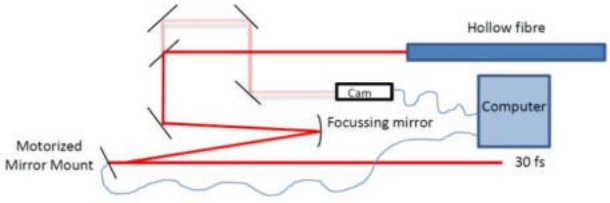

Figure 1 Sketch of the Beam Pointing Stabilization Setup

The camera is connected to a computer and the camera signal is evaluated in a Labview program. Once the beam is at the desired position the beam pointing stabilization can be activated in the Labview program. With the activation the target position of the focal spot is set. An algorithm determines now the centroid position of the focal spot. Deviations from target and actual position are corrected by controlling the voltage of the piezo-crystal equipped mirror mount (Thorlabs) which is placed before the focussing mirror.
In this way it is possible to correct the movement of the beam.

Results

In Figure 2 the results of the beam pointing stabilization are shown. Figure 2 a) shows a long term measurement (16 hours, 42 minutes) of the beam movement without beam pointing stabilization.

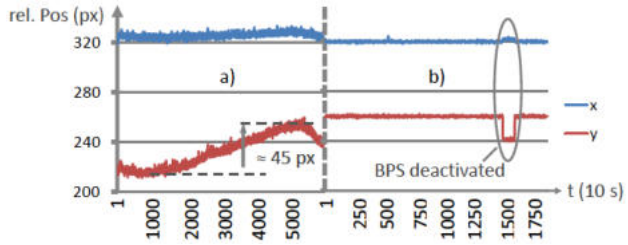

Figure 2 a) Beam movement without BPS
b) Beam movement with BPS

The frame interval was 10 seconds. The y-scale displays the centroid position of the beam in pixel. The blue graph refers to the x and the red graph to the y value of it (accounts also for Figure 2 b)). The data show that the beam favored movement is the y-direction, whereas the x-direction can be almost neglected. Over a time of approximately 12 hours the deviation account to roughly 45 pixels which correspond to 70 µm. Figure 2 b) displays a 5 hours and 10 minutes measurement with activated stabilization. It can be seen that the centroid position of the beam is at a fixed position in x- and y-direction. After 4.16 hours, the beam pointing stabilization was deactivated for a short period of 15 minutes as evidence for a working stabilization system. A deviation appeared and was reduced back to zero when the PBS was re-activated.

Conclusion

The beam pointing stabilization is working well providing a spatially stabilized beam over long periods of time. It has also proven to be a useful tool to align the beam on a day to day basis for the hollow fibre.

References

1. Robinson, Haworth, Teng, Smith, Marangos, Tisch *"The generation of intense, transform-limited laser pulses with tunable duration from 6 to 30 fs in a differentially pumped hollow fibre"* – Applied Physics B 85, 2006

2. WA Bryan et al., *"Few-cycle carrier-envelope-phase controlled laser pulses for time resolved science at the Artemis facility "*, Central Laser Facility Ann Rep 2009-10, RAL-TR-2010-025 (2010)

In-line Flat-field XUV spectrometer for the Artemis beamline

Contact *thomas.kierspel@web.de*

Thomas Kierspel

Carl von Ossietzky University Oldenburg
Niedersachsen, Germany
University of Applied Sciences Emden Leer
Niedersachsen, Germany

Edmond Turcu, Steve Hook, Phil Rice, David Neely, Emma Springate

Central Laser Facility, STFC Rutherford Appleton Laboratory
Didcot, UK

Introduction

The Artemis facility has a monochromatic and a broadband XUV beamline where the XUV beams are generated by femtosecond-laser high harmonic generation (HHG) in a gas jet. The XUV spectrum, stretching between 10-100eV photon energy, is measured with Flat-field (FF) spectrometer in the broad. We have modified the FF-spectrometer design such that the spectrum can be measured in-line by inserting and withdrawing an x-ray mirror during an experiment using the beamline.

General Description

In Figure 1 an engineering drawing of it is shown of part of the Artemis XUV broadband beamline.
The XUV beam is generated in the XUV vacuum chamber. The beam leaves this chamber through a pinhole into the Flat-field chamber. The pinhole is needed to block part of the infrared beam as well for differential pumping of the XUV and Flat-field vacuum chambers.
The XUV beam is then either guided towards the Flat-field spectrometer or it passes through it towards the Relay-Chamber and the interaction chamber.

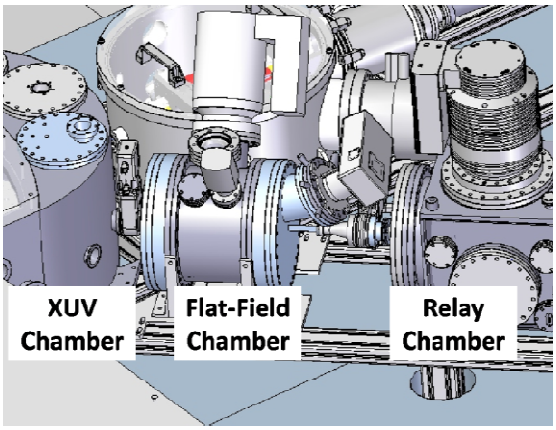

Figure 1 Engineering drawing of the broadband XUV Beamline

Setup Flat Field Spectrometer

An engineering drawing of the inside of the Flat-field chamber is shown in Figure 2. The left part of Figure 2 shows a goniometer stage (Thorlabs) which is placed on top of a linear stage (Thorlabs). The goniometer is equipped with a mirror mount (constructed in-house) which contains two gold X-ray mirrors and is used to shift the incident XUV beam vertically up.

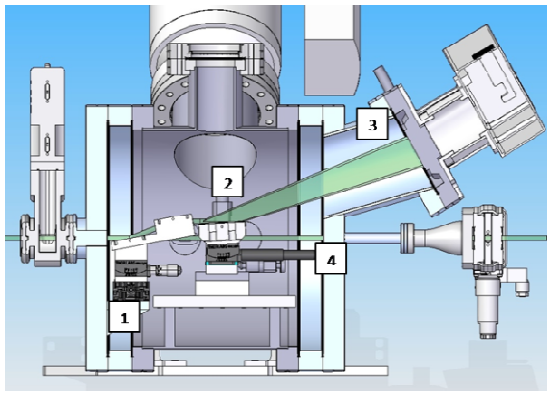

Figure 2 Engineering drawing of the FF-Chamber with

1) Goniometer and mirror mount for liner shift of the beam
2) Grating
3) MCP and photomultiplier
4) Beam if 1) is not in the beam path

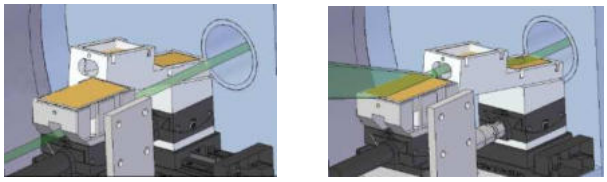

Figure 3 Left: Option 1 beam passes FF chamber Right: Option 2 beam is guided towards spectrometer

The linear stage is used to move the goniometer and the mirror mount in or out of the beam path (Figure 3). If it is in the beam path, the linear shift is used to guide the XUV beam onto a grating. The XUV grating (Hitachi) is a spherical grating with variable-line-spaced grooves to provide a flat focal plane. It has 1200 grooves per mm and is optimized for the wavelength range from 5-20 nm. If the x-ray mirrors are out of the XUV beam path the beam bypasses the Flat-field spectrometer and can be used in the interaction chamber.

Conclusions

We have modified the Flat-field XUV spectrometer design such that the XUV spectrum can be measured in-line by inserting and withdrawing two X-ray mirrors into the XUV beam during an experiment using the beamline.
The chosen setup is a simple and easy solution to do so while an experiment is running.

Modeling of the VMI spectrometer for the Artemis beam line

Contact *m.siano08@ic.ac.uk*

Marco Siano

Imperial College London
South Kensington Campus

SW7 2AZ London UK

Introduction

The recently commissioned AMO endstation at Artemis has been provided with a Velocity Map Imaging[1] spectrometer designed to detect electrons with kinetic energies in the 0-200 eV range. In order to obtain an estimate of the energy resolution for different voltage settings and to determine the maximum kinetic energy detectable extensive simulations have been performed. After a brief introduction on the VMI technique and on the design features of the spectrometers the results of the simulations will be presented.

Velocity Map Imaging

In a VMI spectrometer a cloud of charged particles is projected on a position sensitive detector (PSD) by means of an electrostatic field. The 2D distribution thus obtained represents an image of the momentum distribution of the particles [2] and under certain conditions (cylindrical symmetry) the full 3D momentum distribution can be extracted. In the original design the electrostatic field is created by a set of 3 electrodes commonly referred as repeller, extractor and flight tube (see fig. 1). The interaction region defined as the intersection between the laser beam and the molecular beam has a finite size and this introduce a blurring effect on the image which ultimately affects the momentum resolution. The ratio ρ_{er} between the voltage on the extractor and repeller is adjusted to compensate for this effect: the field lines are gently curved around the interaction region so that particles with the same momentum components (p_x, p_z) hit the detector at the same point regardless of the point within the interaction region where they were generated.

The VMI at Artemis

The VMI spectrometer designed for the AMO chamber at the Artemis has been optimized to measure the momentum distribution of electrons with kinetic energy from 0 up to ~200 eV. Because of the way that the different electrodes are held together it is very simple to change or add electrodes and to modify their distances. This feature accounts for the facility

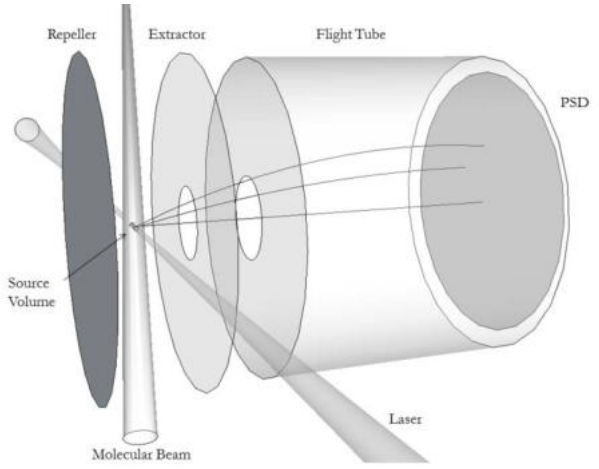

Figure 1: Schematic representation of the electrodes in a VMI spectrometer.

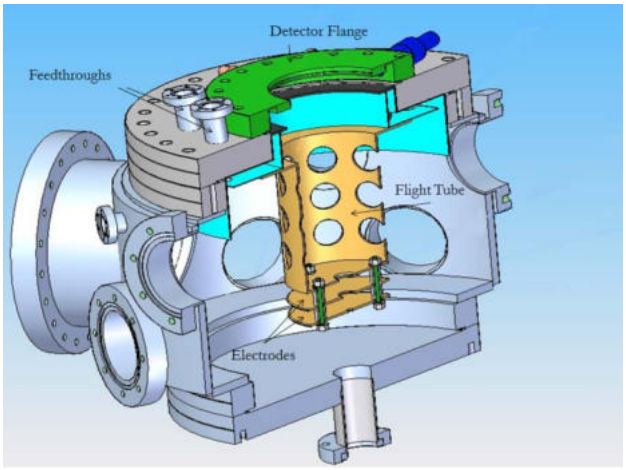

Figure 2: The AMO chamber at Artemis

user nature of Artemis. Different user may have different requirements in terms of electrodes geometry.

If the initial kinetic energy of the particle is much smaller than the kinetic energy acquired in the VMI field the Newton's law yields the following expression for the maximum detectable kinetic energy K:

$$K = \frac{eE}{4L} r_{max}^2$$

where L is the distance between the interaction region and the PSD, r_{max} is the radius of the its active area and E is the electrostatic field (assumed uniform for simplicity). Consequently squat flight tubes and high voltages (and obviously large aperture PSDs) need to be employed to detect high kinetic energy particles. The distance between the interaction region and the PSD detector has been set to 18.5 cm so that electrons with kinetic energies around 200 eV can still be collected when the repeller voltage is at 15 kV which its highest possible value allowed by the voltage supplier. In order to prevent electric discharges which are possible at such a high voltage electropolished electrodes have been employed.

The whole apparatus is enclosed into a double layer of μ-metal in order to cancel the effect of the Earth magnetic field. In order to increase the pumping efficiency holes with a diameter of 2.5 cm have been made in both the flight tube and μ-metal shield.

To operate the spectrometer as a plain VMI only three separate high voltage connections are needed (repeller, extractor, flight tube). However the top flange of the chamber has been designed so that up to 8 feedthroughs can be used and hence 8 different electrodes can be employed. This allows the implementation of more complicated electrostatic fields which are required for techniques such as slice imaging [3].

The electrodes are held together by screws made out of a high voltage and vacuum compatible plastic (Kapton). The spacing between the electrodes is customizable as it is obtained by means of ceramic spacers (MACOR) which sit in four holes on each plate.

The PSD detector is a set of two microchannel plates with pore size of 12 μm and a phosphor screen. The active diameter of the detector is 75 mm. It is possible to run the detector in different voltage configurations according to the voltage applied on the VMI plates and the particles detected. In a commonly used configuration the front surface of the MCP is grounded and the back surface is set to a voltage between 1.7 and 2 kV. The phosphor screen is between 3 and 5 kV above the voltage on the back of the MCP. When a charged particle hits the front of the MCP a cascade of electrons is produced through the channels. The voltage across the plates drives this electron current towards the phosphor screen where a bright spot is produced (luminescence). An image of the phosphor screen is finally captured by a CCD camera.

Simulated performances

An estimate of the performances of the device in terms of maximum kinetic energy detectable and energy resolution has been obtained by performing simulations with SIMION 8 with repeller set at 15 kV and at different values of ρ_{er}. In each simulation the trajectories of a total of $5 \cdot 10^6$ electrons with fixed initial kinetic energies (15,50,100,150,200 eV, 10^6 particles per value) and uniform angular distributions have been calculated. To take into account that the interaction region has a non negligible size the initial position for each particle is assigned randomly according to a 3D Gaussian distribution with σ_x = 1000 μm, $\sigma_y = \sigma_z$ =50 μm where x is the laser propagation direction (see fig. 1). For each simulation the (x,z) coordinates of the particle on the detector are recorded and the simulated image is obtained by binning the particles according to the impact coordinates in 512x512 greyscale images. The images are then inverted using the PBASEX algorithm [4] to obtain the full 3D momentum distribution.

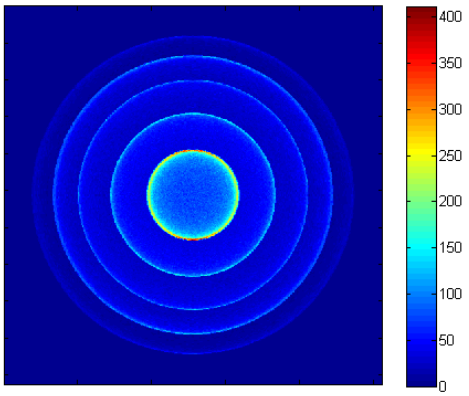

Figure 3: Sample simulated 512x512 VMI image with repeller voltage at 15 kV. The rings correspond to electrons with kinetic energies of 15,50,100,150 and 200 eV.

The figure above shows a typical simulated image. Each concentric ring corresponds to the projection on the detector plane of a set of monoenergetic electrons with uniform angular distribution, i.e. a sphere in the momentum plane.

In general there is no unique value of ρ_{er} that ensures an optimum focusing for every choice of the initial kinetic energy of the particles. In order to assess the extent of this effect simulations analogous to the one in fig. 3 have been run for different values of ρ_{er}. The results are summarized in fig. 4.

From each of the inverted images the radial distribution is calculated. For a device with perfect energy resolution and for monoenergetic particles the radial distribution should be the equivalent of a discrete Dirac delta function, i.e. a distribution which is non zero only at a specific radial pixel. Real spectrometers, however, have a finite resolution and consequently each peak results in a radial distribution which has roughly the shape of a Gaussian. The relative radial resolution

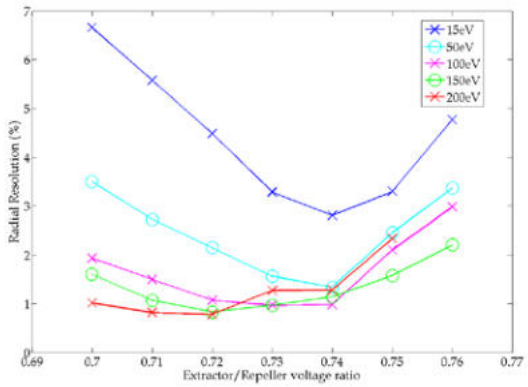

Figure 2: Relative radial (momentum) resolution as a function of ρ_{er} for different kinetic energies.

is calculated by finding the FWHM in pixels of the curve and dividing it by the position of the maximum.

From figure 4 it can be seen that for energies up to 50 eV the best focusing is achieved for ρ_{er} =0.74. Then the focusing condition moves to ρ_{er} = 0.72 for energies of 150 eV and 200 eV.

In order to obtain an estimate of the energy resolution an energy calibration needs to be performed. For each value of ρ_{er} the positions in radial pixels of each peak are fitted with the function

$$\boldsymbol{px = aE^{\alpha}}$$

In figure 5 the results of this procedure are summarized and the values for a and α for different voltages are reported.

It can be shown that for a set of monoenergetic particles the relationship between its energy and the maximum radius of the circle on the detector is quadratic and hence the value of α is expected to be around 0.5.

The conversion from radial pixels to energy performed for the voltages for which the focusing is optimum at different energies yields the following values for the relative energy resolutions R:

$$R_{15eV} = 5.83\%$$
$$R_{50eV} = 2.77\%$$
$$R_{100eV} = 2.02\%$$
$$R_{150eV} = 1.72\%$$
$$R_{200eV} = 1.61\%$$

In order to obtain the maximum kinetic energy detectable it is sufficient to reconvert the formulas in fig. 5 in energy as a function of the actual distance from the center of the detector. The pixel-to-distance in mm conversion factor used in the simulations is 0.1406. Using this value we obtain the following relationship for energy as a function of radius in mm

$$E(\text{eV}) = 0.1657\ [r\ (\text{mm})]^{2.0636}$$

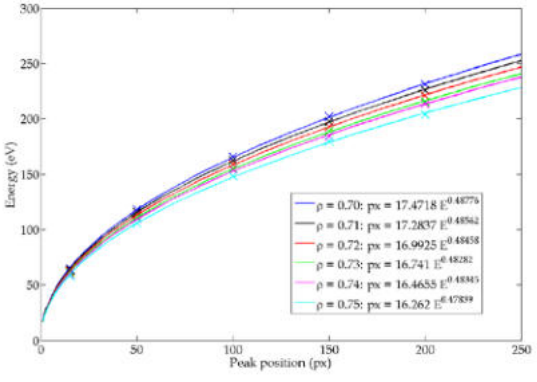

Figure 3: Pixel-to-energy calibration curves for different values of ρ_{er}.

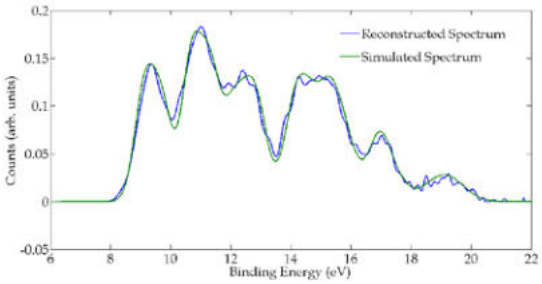

Figure 4: Simulated and reconstructed (after Abel inversion of the simulated image) photoelectron spectra of bromobenzene based on the one obtained in [5] with HeI radiation but convoluted with a Gaussian of σ=0.3 eV. (V_{repeller} = 15 kV, ρ_{er} = 0.72)

which gives a maximum kinetic energy detectable

$$E_{\max} = E(\text{r} = 32.5 \text{ mm}) = 218 \text{ eV}.$$

In order to see the combined effect of the finite energy resolution of the spectrometer and the possible distortion of the spectrum introduced by the inversion procedure a realistic photoelectron spectrum has been simulated. The reference is provided by the photoelectron spectrum of bromobenzene ionized with HeI radiation [5]. The experimental spectrum has been extracted in the form of a series of Gaussians and then convoluted with a Gaussian of σ=0.3 eV. This has been done in order to reproduce the ionization by the VUV source available at Artemis. The areas under each Gaussian in the final spectrum have been taken as a reference to assign the number of particles for each peak.

From fig. 6 we can see that the agreement of the reconstructed spectrum with the simulated one is reasonable. Minor discrepancies are due to an insufficient number of particle trajectories simulated. The conclusion is that the spectrometer is capable of measuring photoelectron spectra with a similar level of complexity provided that the number of counts is high enough.

Conclusions

The SIMION 8 simulations of the VMI spectrometer at Artemis show that the device has been optimized for the detection of high kinetic energy electrons. The expected energy resolution for 200 eV electrons is 1.61%. For lower kinetic energy electrons the resolution is sensibly worse and it is expected to introduce some distortions when a photoelectrons spectrum extending on the whole detector is recorded. However, the simulation of a realistic spectrum (see fig. 6) has shown that the distortion is minimal.

Acknowledgments

The design and the realization of the VMI spectrometer has been carried out with the technical help from S. Spurdle, T. Strange, P. Rice and Steve Hook (Central Laser Facility) and the supervision of Dr. J. Underwood (University College London), Dr E. Springate (Central Laser Facility, STFC RAL) and Prof. J. P. Marangos (Imperial College London).

References

1. A. T. J. B. Eppink and D. Parker, *Rev. Sci. Instrum.* **68** (9), 3477 (1997).
2. C. Bordas, F. Paulig, H. Helm, and D. L. Huestis, *Rev. Sci. Instrum.* **67**, 2257 (1996).
3. D. Townsend, M. P. Minitti, and A. G. Suit, *Rev. Sci. Instrum.* **74**, 2530 (2003).
4. G. A. Garcia, L. Nahon and I. Powis, *Rev. Sci. Instrum* **75** (11), 4989 (2004).
5. D.M.P. Holland, D. Edvardssonb, L. Karlssonb, R. Maripuuc, K. Siegbahnc, A.W. Pottsd, W. von Niessene, *Chemical Physics* **252** (1-2), 257 (2000).

Improvements to the Artemis Facility Interlock System

Contact *Edmond.Turcu@stfc.ac.uk*

A. Tylee, S. Tomlinson, R. Bickerton, E. Springate & E. Turcu

Central Laser Facility
STFC Rutherford Appleton Laboratory, Didcot, OX11 0QX

Introduction

The Artemis laser system requires time to stabilise before the laser can be used. Prior to the interlock upgrade, the lab was rendered hazardous during this time. It was necessary for any personnel entering the area to wear the appropriate goggles, which was particularly prohibitive to engineers and users working on and setting-up experiments at the interaction chamber. There was a partial interlock system for the first lidded enclosure, but this required manual overrides and loss of power to the laser to enable the override. The new interlock system has enclosed a larger portion of the laser system and lid overrides can be enabled from the control panel. Therefore there is better access for engineering staff and users whilst the laser is stabilising or operational. There has also been a significant improvement to the ease of use of the interlock system, saving much time and effort for the laser scientists.

Laser System

The Artemis laser system consists of the Red Dragon Laser System (a laser oscillator, two laser amplifiers, three pump lasers) emitting 800nm, 30fs, 14mJ, 1KHz radiation and a TOPAS tunable laser emitting from 240nm UV to 20,000nm mid-range IR. The pump lasers emit 30 to 40 W of 532nm green radiation.

Mechanical Enclosures

The upgraded interlock system encloses the whole laser system described above and segregates it into 3 areas by the use of shutters (Fig 1). A portion of the enclosures are fixed and cannot be opened in normal operation. The remaining enclosures have access lids which are linked to the control system via magnetic switches and can be overridden by authorised persons.

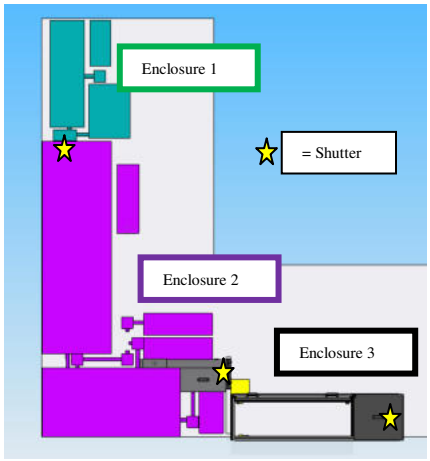

Figure 1: Enclosure Segregation - Mechanical Schematic

Shutters

The second enclosure required three controlled outputs in a small spatial area. A bespoke shutter (Fig. 2) was designed to suit and incorporated into the interlock control system. The design was a simple pneumatically operated barrier plate in each output position, which closed under gravity to ensure it fails safe.

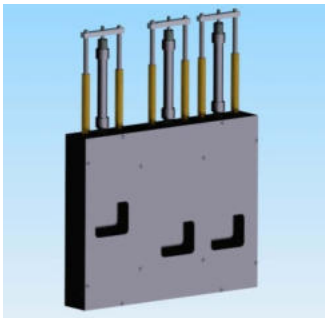

Figure 2: Shutter

Interlock Hardware

The existing electrical interlock hardware has been reconditioned and upgraded. Dedicated power supplies and additional hazard screens have been installed. The cable routing has been rationalized to improve the presentation of the lab and unused cables have been removed.

PLC Logic Improvements

Software changes have been made to future proof and simplify the task of displaying lasers on the Cerberus hazard screens (Fig. 3).

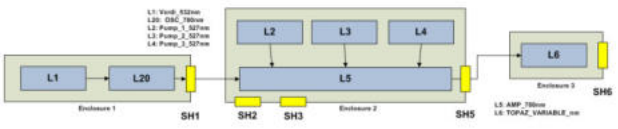

Figure 3 –Lasers and Their Enclosures - Software Screen

Multiple lasers can reside in a single enclosure. The propagation of different wavelength lasers into downstream enclosures is controlled via the shutters. The hazard screens then display the appropriate accumulation of hazards dependent upon which shutters are open.

The new hazard table can be directly converted into PLC logic (Fig. 4).

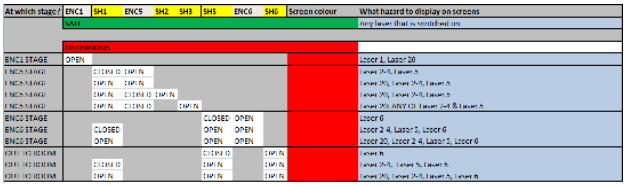

Figure 4 –Artemis Laser Hazard Software Table

The code separation between the PLC main program logic and the Cerberus logic (Fig 5.) is easily identifiable and thus more easily supported. This approach to PLC design shall be utilised in other forthcoming lab developments in the CLF.

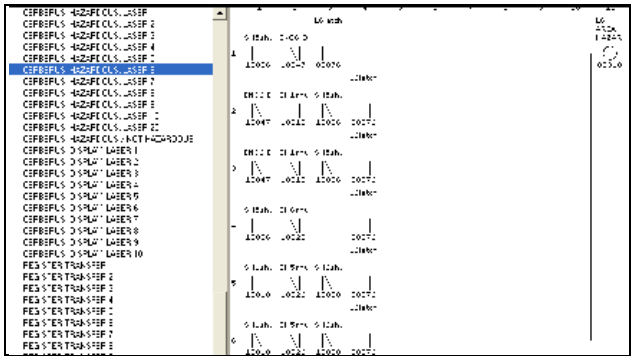

Figure 5 – Cerberus PLC Logic Design

Conclusions

The upgrade to the Artemis interlock system has significantly improved the usability of the Artemis lab for engineering staff and users of the area as well as the laser stability. The lab can now be accessed without goggles by closing the laser-output-shutters rather than switching the laser off. Therefore the laser is kept warm and stable so that the experimental measurements can be resumed, on request, within a few minutes rather than hours. This provides an important time saving as well as making the area as safe as possible for the users of the lab.

Authorised personnel are permitted to access the lasers within the enclosures, which is controlled by an access key on the control panel. The time taken to open and close the enclosure lids during laser alignment is much reduced by the improved lid interlock override button on the control panel.

The interlock system is now easier to use for the laser scientists and provides improved hazard warning and safety information for all users of the Artemis lab. An additional benefit of the upgrade is that the system is more easily supportable by the electrical engineering group.

Acknowledgements

The interlock upgrade work was instigated and requirements specified by Emma Springate and Edmond Turcu.

The mechanical system of the interlock upgrade was manufactured and installed by Mick Selley, Andy Jackson, John Monk and Alan Ryder.

The electrical system of the interlock upgrade was installed by Lee Hall and Graham Wiggins.